ISSN 1560-3547, Regular and Chaotic Dynamics, 2017, Vol. 22, No. 6, pp. 700–720. © Pleiades Publishing, Ltd., 2017.

Diffusion and Drift in Volume-Preserving Maps

Nathan Guillery* **and James D. Meiss****

Department of Applied Mathematics, University of Colorado Boulder
Boulder, CO 80309-0526

Received September 13, 2017; accepted October 18, 2017

Abstract—A nearly-integrable dynamical system has a natural formulation in terms of actions, y (nearly constant), and angles, x (nearly rigidly rotating with frequency $\Omega(y)$). We study angle-action maps that are close to symplectic and have a twist, the derivative of the frequency map, $D\Omega(y)$, that is positive-definite. When the map is symplectic, Nekhoroshev's theorem implies that the actions are confined for exponentially long times: the drift is exponentially small and numerically appears to be diffusive. We show that when the symplectic condition is relaxed, but the map is still volume-preserving, the actions can have a strong drift along resonance channels. Averaging theory is used to compute the drift for the case of rank-r resonances. A comparison with computations for a generalized Froeschlé map in four-dimensions shows that this theory gives accurate results for the rank-one case.

MSC2010 numbers: 37J40, 70H08, 34C28, 37C05

DOI: 10.1134/S1560354717060089

Keywords: symplectic maps, Nekhoroshev's theorem, chaotic transport

1. INTRODUCTION

Arnold noted in his 1964 famous paper, "Instability of Dynamical Systems with Several Degrees of Freedom", that the stability of an elliptical equilibrium in a Hamiltonian system with three or more degrees of freedom is not guaranteed [1]. Of course, transport in typical, nearly-integrable Hamiltonian systems, and correspondingly in symplectic maps, is inhibited because — by KAM theory — much of the phase space is foliated by invariant tori on which the dynamics is quasi-periodic [2–4]. In addition, Nekhoroshev showed that in certain cases — as we review in Section 2 — the transport in chaotic regions of phase space is also small on an exponentially long time scale [5, 6], implying a "quasi-stability" of the dynamics, i. e., that the "Arnold diffusion" is exponentially small. We will show that this quasi-stability can dramatically fail for a volume-preserving map that is "nearly" symplectic.

In this paper we will study transport in maps $(x', y') = f(x, y; \varepsilon)$ on $\mathbb{T}^d \times \mathbb{R}^k$, with d angle and k action variables that are volume-preserving but need not be symplectic. One well-studied example of such a map is a volume-preserving discretization of the Arnold – Beltrami – Childress flow [7], called the "ABC map" [8]; if two parameters of this three-dimensional map are small, it can be thought of as having two angles and one action.

We assume that the map f has a formal parameter ε, such that when $\varepsilon = 0$ the actions are constant and the angles undergo a rigid rotation, with an action-dependent rotation vector. It is convenient to write such a map in the form

$$\begin{aligned} x' &= x + \Omega(y') + \varepsilon X(x, y; \varepsilon), \\ y' &= y + \varepsilon Y(x, y; \varepsilon). \end{aligned} \tag{1.1}$$

*E-mail: Nathan.Guillery@Colorado.EDU
**E-mail: James.Meiss@Colorado.EDU

Here $\Omega : \mathbb{R}^k \to \mathbb{R}^d$, the *frequency map*, is evaluated at the image point $y'(x, y)$, and $X : \mathbb{T}^d \times \mathbb{R}^k \to \mathbb{T}^d$ and $Y : \mathbb{T}^d \times \mathbb{R}^k \to \mathbb{R}^k$ are perturbing "forces". For the simplest case we set $X \equiv 0$ and $Y(x, y; \varepsilon) = F(x)$ to be independent of the actions, giving

$$\begin{aligned} x' &= x + \Omega(y'), \\ y' &= y + \varepsilon F(x). \end{aligned} \tag{1.2}$$

This form is volume-preserving for any smooth Ω and F, see Section 2. It generalizes Chirikov's area-preserving map (where $d = k = 1$) [9], Froeschlé's symplectic map (where $d = k = 2$) [10], and the volume-preserving normal form for a rank-one resonance ($d \geqslant 2$, $k = 1$) [11].

The maps (1.1) and (1.2) are integrable whenever $\varepsilon = 0$ in the sense that the actions are constant so that each d-torus $\mathcal{T}_y = \{(x, y) \,|\, x \in \mathbb{T}^d\}$ is invariant. In this case the angles evolve by rigid rotation with the rotation vector $\Omega(y)$. Denoting orbits of the map by sequences $\big(x^{(t)}, y^{(t)}\big) = f^t\big(x^{(0)}, y^{(0)}\big)$, the dynamics of the integrable case are

$$\big(x^{(t)}, y^{(t)}\big) = \big(x^{(0)} + \omega t,\ y^{(0)}\big), \tag{1.3}$$

with the fixed rotation vector $\omega = \Omega\big(y^{(0)}\big)$. When ω is incommensurate, the orbit is dense on the d-torus, $\mathcal{T}_{y^{(0)}}$.

A prominent feature of the dynamics of (1.2) are resonances. Generalizing (1.3), the rotation vector $\omega \in \mathbb{R}^d$ of an orbit $\{\big(x^{(t)}, y^{(t)}\big) : t \in \mathbb{Z}\}$ is obtained by lifting the angle variable to $\mathbb{R}^d$ and computing

$$\omega\big(x^{(0)}, y^{(0)}\big) = \lim_{t\to\infty} \frac{1}{t}\big(x^{(t)} - x^{(0)}\big)$$

if the limit exists. The orbit is said to be in a resonance if ω satisfies at least one relation of the form $m \cdot \omega = n$ for $m \in \mathbb{Z}^d \setminus \{0\}$ and $n \in \mathbb{Z}$. For a given ω, the set of all vectors m that satisfy such a relation,

$$\mathcal{L}(\omega) = \{m \in \mathbb{Z}^d : m \cdot \omega \in \mathbb{Z}\}, \tag{1.4}$$

is called the *resonance module*. For an *incommensurate* frequency $\mathcal{L}(\omega) = \{0\}$. The invariant tori of KAM theory are strongly incommensurate — they satisfy a Diophantine condition. If $\dim \mathcal{L}(\omega) > 0$, then the frequency is *commensurate*. The *rank* of a resonance is the dimension of $\mathcal{L}(\omega)$, the number of independent, resonant m-vectors. Of course, when $\varepsilon = 0$ for (1.2), $\omega = \Omega(y)$, every initial condition on the sets $m \cdot \Omega(y) = n$ is resonant. The existence of resonances has a profound effect on the dynamics.

Though it is clear that when $\varepsilon \ll 1$ the actions evolve slowly under (1.2), there can be stronger constraints on the action dynamics for long or for infinite times. One such constraint is due to KAM theory [3, 4]. A version of the KAM theorem has been proven for real analytic maps of the form (1.2) with one action ($k = 1$) in [12, 13] and for multiple actions in [14]. These theorems imply, under a Rüssmann-type nondegeneracy condition on Ω and an intersection property on F, that there is a Cantor set of invariant tori when $\varepsilon \ll 1$. The intersection property is the requirement that every d-torus sufficiently close to the constant torus $\mathcal{T}_y$ intersects its image. When $k = 1$, the codimension-one KAM tori constrain transport: no trajectories can cross such a torus.

However, when $k > 1$, the existence of codimension-k tori no longer implies eternal stability, leading to the famous Arnold instability mechanism [1]. Nevertheless, when a map of the form (1.1) is symplectic, Nekhoroshev's theorem, which we recall in Section 2, can imply long time stability. In a symplectic map, the angle and action variables are canonically paired, so one must have $k = d$. Moreover, as we discuss in Section 2, when (1.2) is (canonically, exact) symplectic, the force must be conservative:

$$F(x) = -\nabla V(x), \tag{1.5}$$

for some potential $V : \mathbb{T}^d \to \mathbb{R}$, and the frequency must be generated by a function $S : \mathbb{R}^d \to \mathbb{R}$:

$$\Omega = \nabla S(y).$$

It is most common to assume that $S(y) = \frac{1}{2}\|y\|^2$, so that Ω is the identity map. There have been many studies of transport in the symplectic case ranging from early studies [15–17] to more recent results [18–25].

In this paper we we will compare the dynamics of symplectic and volume-preserving maps of the form (1.2) for the four-dimensional case, $k = d = 2$, with

$$\Omega(y) = y,$$
$$F(x) = -\frac{1}{2\pi}\begin{bmatrix} a\sin(2\pi x_1) + c\sin\big(2\pi(x_1+x_2)\big) \\ b\sin(2\pi x_2) + c\sin\big(2\pi(x_1+x_2+\varphi)\big) \end{bmatrix}. \tag{1.6}$$

Here the terms with amplitudes a, b, and c represent forcing of the $(1,0,n)$, $(0,1,n)$, and $(1,1,n)$ resonances, respectively. Note that F is a gradient only when the phase $\varphi = 0 \mod 1$. This case is Froeschlé's symplectic map [10], and Nekhoroshev's theorem (see Theorem 1) applies. The case that $\varphi = \frac{1}{2}$ and $b = 0$ in (1.6) has also been studied previously, beginning with the work of Pfenniger [26] on the Hamiltonian-Hopf bifurcation, see also [27, 28]. Though the force for $\varphi = \frac{1}{2}$ is not a gradient, the map becomes symplectic under a noncanonical coordinate transformation of the form $(x_1, x_2, y_1, y_2) \to (x_1, x_2, y_1, -y_2)$ (however, this makes the twist indefinite, see Section 2). We will use φ as a convenient parameter to measure the deviation from symplecticity.

At the simplest level, Nekhoroshev's quasi-stability for (1.2) is related to the fact that when an orbit is in an $m \cdot \Omega(y) = n$ resonance, the most important terms in the Fourier expansion of the force are those that have the angle dependence $m \cdot x$, since these vary slowly. When the force is a gradient (1.5), then the resonant Fourier terms in F are of the form

$$\tilde{F}_m \propto m\sin(2\pi m \cdot x + \theta),$$

that is, they are in the m direction. However, if $\Omega(y) = y$, then m is orthogonal to the resonance manifold, $m \cdot y = n$, and the dynamics induced by the resonant force will be small, pendulum-like oscillations transverse to the resonance. The more profound result of Nekhoroshev is that the motion along resonance manifolds is in fact exponentially slow. By contrast, when F is not a gradient, the resonant force can be in any direction, and in particular can have components along the resonance manifold, causing strong drifts, as we will see in Section 3. We will extend the argument above to more general frequency maps in Section 4, then apply first-order averaging theory to compute these drifts in Section 5, and finally show that this calculation agrees with numerical simulations in Section 6.

2. SYMPLECTIC AND VOLUME-PRESERVING MAPS

Though the angle-action map (1.2) is not always symplectic, it always preserves volume: there is a volume form $\mathcal{V}$ such that $f^*\mathcal{V} = \mathcal{V}$. Indeed, for any smooth frequency map and force, (1.2) preserves the standard volume,

$$\mathcal{V} = dx_1 \wedge dx_2 \wedge \ldots \wedge dx_d \wedge dy_1 \wedge \ldots \wedge dy_k, \tag{2.1}$$

so that volume preservation is equivalent to $\det Df = 1$, where Df is the Jacobian. This is easiest to see by writing the map as the composition $f = f_2 \circ f_1$ where

$$f_1(x,y) = \big(x, y + \varepsilon F(x)\big) \qquad \text{and} \qquad f_2(x,y) = \big(x + \Omega(y), y\big)$$

are shears. Much of the study of the dynamics of volume-preserving maps has concentrated on three-dimensional maps $k + d = 3$, especially for "one-action" ($k = 1$) and "two-action" ($k = 2$) [8, 29, 30] cases.

For the most of this paper, we will assume that $d = k$: the number of angle and action variables are the same and $(x, y) \in \mathbb{T}^d \times \mathbb{R}^d$. This is especially appropriate for symplectic maps where each angle variable x_i is canonically paired with an action variable y_i. In the canonical case the map preserves the two form $\sigma = dy \wedge dx = \sum_{i=1}^{d} dy_i \wedge dx_i$; that is, f is symplectic when $f^*\sigma = \sigma$ [31], or

$$Df^T J Df = J, \qquad J = \begin{pmatrix} 0 & -I \\ I & 0 \end{pmatrix}, \tag{2.2}$$

where is J the $2d \times 2d$ Poisson matrix[1)]. Every such symplectic map preserves the $2d$-volume form (2.1).

The generalized Froeschlé map (1.2) has Jacobian

$$Df(x,y) = \begin{pmatrix} I + \varepsilon D\Omega\big(y + \varepsilon F(x)\big) DF(x) & D\Omega\big(y + \varepsilon F(x)\big) \\ \varepsilon DF(x) & I \end{pmatrix}. \tag{2.3}$$

This matrix satisfies (2.2) only when the $d \times d$ matrices DF and $D\Omega$ are symmetric. Indeed, setting the formal parameter $\varepsilon = 1$ and dropping the arguments from $D\Omega(y')$ and $DF(x)$ gives

$$Df^T J Df = \begin{pmatrix} DF^T - DF + DF^T(D\Omega - D\Omega^T) & -I + DF^T(D\Omega - D\Omega^T) \\ I + (D\Omega - D\Omega^T)DF & D\Omega - D\Omega^T \end{pmatrix}.$$

In order that this reduce to J, the lower right block must vanish, so $D\Omega$ is symmetric, and then vanishing of the upper left block implies that DF is also symmetric. More remarks about the symplecticity of (1.2) and its symmetries are in Appendix A and B.

A special category of symplectic maps are the *exact* maps. The symplectic form σ on $\mathbb{T}^d \times \mathbb{R}^d$ is exact: there is a Liouville one-form $\nu = y \cdot dx$, so that $\sigma = d\nu$. A map f is exact symplectic with respect to ν if there exists a discrete *Lagrangian* $L(x, y, x', y')$ such that

$$f^*\nu - \nu = y' \cdot dx' - y \cdot dx = dL \tag{2.4}$$

on the graph $(x', y') = f(x, y)$. Of course, every such map is also symplectic since $d(f^*\nu) - d\nu = f^*\sigma - \sigma = d^2 L = 0$. In order that the map be well-defined on the torus, $L(x + m, y, x' + m, y') = L(x, y, x', y')$ for each $m \in \mathbb{Z}^d$. For example, if

$$L(x, y, x', y') = (x' - x) \cdot y' - S(y') - \varepsilon V(x), \tag{2.5}$$

for a periodic potential V, then rearranging (2.4) gives $x' \cdot dy' + y \cdot dx = d\big(x \cdot y' + S(y') + \varepsilon V(x)\big)$, or equivalently

$$\begin{aligned} x' &= x + \nabla S(y'), \\ y' &= y - \varepsilon \nabla V(x). \end{aligned} \tag{2.6}$$

This is the generalized Froeschlé map (1.2) with the force $F(x) = -\nabla V(x)$ and frequency map $\Omega(y) = \nabla S(y)$. Of course, in this case DF and $D\Omega$ are automatically symmetric.

When $\varepsilon = 0$, the map (2.6) is integrable in the sense of Liouville: the d-action variables are invariants. As we noted in Section 1, the dynamics on each d-dimensional torus corresponds to rigid rotation with rotation vector $\omega = \Omega(y)$. The *twist* of the map is the symmetric matrix $D\Omega = D^2 S$, and the map is said to have *positive-definite twist* on a set $B \in \mathbb{R}^d$ when $D\Omega$ is uniformly positive definite; i. e., when there exists a $C > 0$ such that

$$v^T D\Omega(y) v \geqslant C\|v\|^2, \quad \forall y \in B. \tag{2.7}$$

In this case the frequency varies nontrivially from torus-to-torus.

In certain cases, the orbits of (2.6) do not stray too far from this integrable case when $\varepsilon \ll 1$. In particular, for the symplectic case, Nekhoroshev's theorem asserts that the actions of *all* orbits do not drift far over exponentially long times. Although originally proven for Hamiltonian flows [5], Nekhoroshev's theorem applies to exact symplectic maps by flow interpolation [32]. It was also proven directly for the positive-definite twist case by Guzzo:

[1)] More generally, σ is only required to be a nondegenerate two-form, though Darboux's theorem implies that there are local canonical coordinates [31].

Theorem 1 ([33]). *Suppose that $B \subset \mathbb{R}^d$ is an open set, $S : B \to \mathbb{R}$, and $V : \mathbb{T}^d \to \mathbb{R}$ are analytic, and $D\Omega = D^2 S$ is uniformly positive definite on B. Then for orbits of* (2.6) *there exist positive constants $\varepsilon_0, \alpha, \beta, T_0, C_0$ such that for any $\varepsilon < \varepsilon_0$, and for any $\left(x^{(0)}, y^{(0)}\right) \in \mathbb{T}^d \times B'$, with $B' = \{y \in B : dist(y, \partial B) > 2C_0\varepsilon^\alpha\}$,*

$$\|y^{(t)} - y^{(0)}\| \leqslant C_0 \varepsilon^\alpha$$

for any $t \in \mathbb{Z}$ satisfying

$$|t| \leqslant T_0 \exp\left(\frac{\varepsilon_0}{\varepsilon}\right)^\beta.$$

Informally this theorem implies that the drift in the action variables is very slow. The exponents obtained vary, depending upon the methods used to prove the theorem, but typically $\alpha \leqslant \frac{1}{2}$, the upper limit being determined by the width of typical resonances, and $\beta \simeq (2d)^{-1}$.

In the next sections, we will contrast the action transport for the map (1.2) when it is constrained by Theorem 1, with the action transport when the map is only volume-preserving but still satisfies the remaining hypotheses of Theorem 1.

3. VISUALIZING TRANSPORT AND DRIFT

The visualization of the dynamics of a four or higher-dimensional map is a challenge. A key numerical tool is to compute some scalar quantity on strategically chosen two-dimensional slices of initial conditions. To delineate chaotic regions one would like to compute the largest Lyapunov exponent; however, it is difficult to obtain accurate results. A more well-behaved quantity is the Fast Lyapunov Indicator (FLI) [22, 34],

$$\gamma\left(x^{(0)}, y^{(0)}; v, T\right) = \sup_{\tau \leqslant T} \log \left\| \prod_{t=0}^{\tau-1} Df\left(x^{(t)}, y^{(t)}\right) v \right\|, \tag{3.1}$$

where v is some fixed deviation vector. The use of the supremum allows the FLI to distinguish orbits using a smaller number of iterations, T, than needed for the Lyapunov exponent to converge. As a first illustration consider the decoupled case $c = 0$ for (1.6). In each canonical plane the map is then an area-preserving Chirikov map. The FLI for the (x_1, y_1) plane with $\varepsilon a = 0.52$ is shown in Fig. 1. The color bar shows the range $1 \leqslant \gamma \leqslant 10$ for the FLI (3.1). The highest FLI values occur in the chaotic separatrix layer surrounding the $(0, 1)$ resonance. As noted in [35], the FLI also distinguishes between resonant (dark blue) and rotational (KAM) invariant (light blue) circles.

We can similarly visualize the structure of the phase space in four-dimensions by simultaneously plotting the FLI on several complementary planes of initial conditions [36]. We show three planes for the symplectic Froeschlé map, assembled into faces of a cube, in Fig. 2. The two vertical planes are canonical: the left face is the two-plane $(x_1, 0.0, y_1, 0.65)$ and the right face is the two-plane $(0, x_2, 0.65, y_2)$. Each of these canonical planes has resonant structures resembling the 2D case of Fig. 1, though the amplitudes of the $(0, 1, 0)$ and $(1, 0, 0)$ resonances are smaller here since $\varepsilon a = \varepsilon b = 0.1$. A new feature is a large resonant island that appears in each canonical plane near $y_i = 0.35$. This corresponds to the $(1, 1, 1)$ resonance driven by the coupling with amplitude $\varepsilon c = 0.07$ in (1.6). For example, since $y_2 = 0.65$ on the (x_1, y_1) plane, the zero-order resonant condition $y_1 + y_2 = 1$ corresponds to $y_1 = 0.35$. In the figure, the two canonical planes appear to be artificially joined along a "line" — this is really the two-plane $y_1 = y_2 = 0.65$.

The third, horizontal two-plane in Fig. 2 is the action plane $(0, 0, y_1, y_2)$. It is shown intersecting each canonical plane along the appropriate fixed-angle lines. In the action plane, each rank-one resonance becomes a strip centered on $m \cdot y = n$ with a width proportional to the square root of the amplitude of the resonant term in the force. In this plane, we see prominent strips for the $(1, 0, 0)$, $(0, 1, 0)$, $(1, 1, 0)$ and $(1, 1, 1)$ resonances, as well as a number of smaller resonant strips caused by nonlinear beating. Resonance overlap near the rank-two crossings of these resonances causes stronger chaotic regions. Such overlap necessarily occurs even for very small perturbations, and can cause drift along, and transfer between, resonances. It is the speed of this drift that is addressed by Theorem 1.

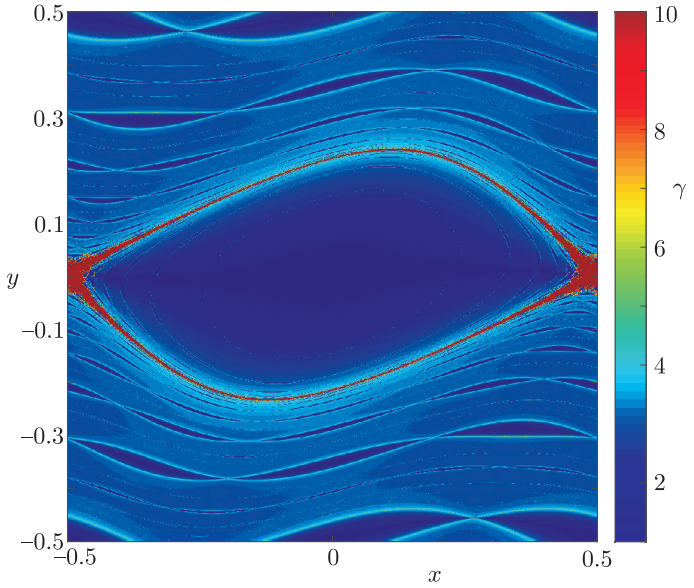

Fig. 1. Fast Lyapunov indicator (FLI) as a function of initial condition for the 2D Chirikov map with $\varepsilon a = 0.52$, with 10^6 initial conditions on a square grid, each iterated $T = 10^3$ steps. The bar (color online) indicates the values of (3.1) for $v = \left((3-\sqrt{5})/2, 1\right)$.

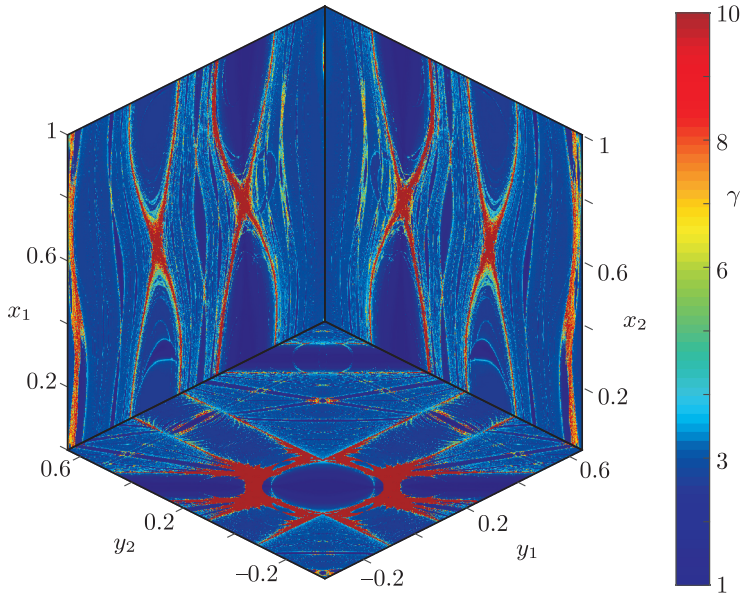

Fig. 2. Three FLI planes for the symplectic ($\varphi = 0$) Froeschlé map with (1.6) for $\varepsilon(a, b, c) = (0.1, 0.1, 0.07)$: an action plane with fixed angles $x_1 = x_2 = 0$, and two canonical planes with the other angle-action pair fixed at $(x_j, y_j) = (0, 0.65)$, with 10^6 initial conditions on each square grid, each iterated $T = 10^3$ steps using $v = ((3-\sqrt{5})/2, 1, 1, 1)$.

These FLI cross-sections provide a look at the global structure of phase space, and can serve as a backdrop for orbit projections. For the symplectic case, orbits within or near a rank-one resonance oscillate orthogonally to the resonance, and Theorem 1 ensures any $\mathcal{O}(1)$ drift parallel to resonances must occur over exponentially long times. Numerical studies have found that this slow process is diffusive [23] (see also Fig. 6 below).

No such long-time stability appears to exist for volume-preserving, nonsymplectic maps. Indeed, when the phase shift φ is nonzero for the generalized Froeschlé map, orbits in the $(1, 1, n)$ resonances

drift rapidly in action space, moving an $\mathcal{O}(1)$ distance in a few hundred iterates. A first indication of this drift is visible in the FLI planes shown in Fig. 3. In this figure the parameters (a, b, c) are half the size of those in Fig. 2; nevertheless, when $\varphi \neq 0$, much of the resonance structure seen in the symplectic case is still present. However, the FLI plots indicate much stronger "chaotic zones", where $\gamma \simeq 6$, in the $(1, 1, 0)$ and $(1, 1, 1)$ resonances. One must be cautious in attributing this to local structure in the map: the actions in these resonances drift far from their initial values.

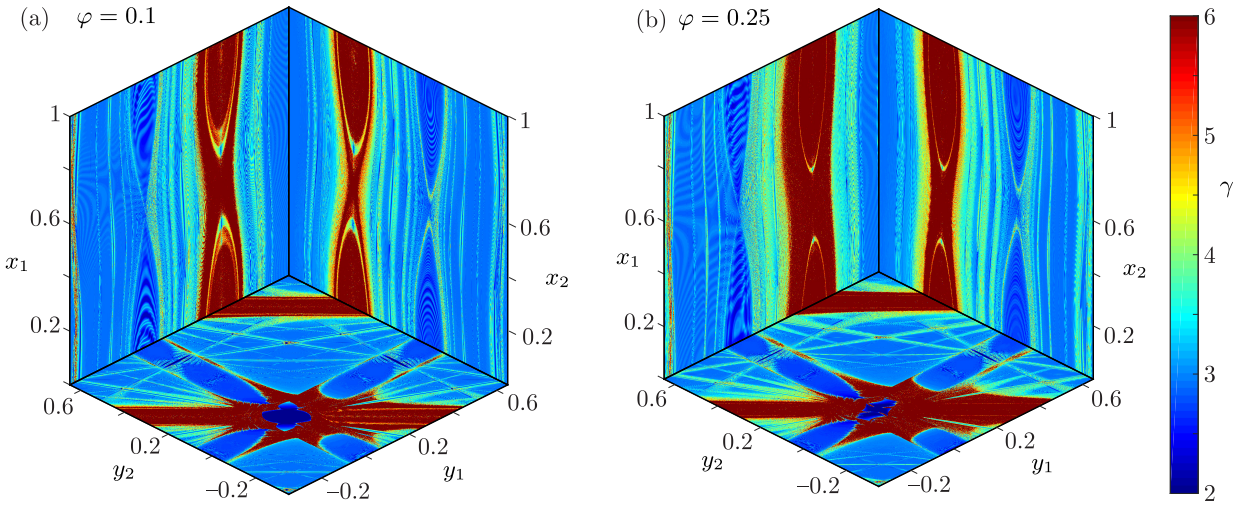

Fig. 3. FLI planes (as in Fig. 2) for the volume-preserving generalized Froeschlé map with $\varepsilon(a, b, c) = (0.05, 0.05, 0.035)$ and $\varphi = 0.1$ (a) and 0.25 (b). The 10^6 initial conditions on each plane are each iterated 10^3 times.

Indeed, one can visualize the drift on the action plane $(0, 0, y_1, y_2)$ by looking at some representative orbits. In Fig. 4, the FLI is shown as a grayscale background, with black for $\gamma = 0$ and white for $\gamma = 6$. For the symplectic case (panel (a)) three orbits were initialized (small dots in green online) in the chaotic separatrix layer of three different resonances, $(1, 1, 0)$ (gold), $(0, 1, 0)$, (red) and $(1, 0, 0)$ (blue). Each initial condition was iterated 10^{10} times, and points are plotted only when $|x_1|, |x_2| < 0.001$. Note that the orbits are confined to a small interval of size $\mathcal{O}(0.1)$ along the resonance and to a narrow chaotic zone that appears in the slice to be two sides of the separatrix layer of the resonance.

By contrast, when $\varphi \neq 0$, the orbits drift along the resonances rapidly as shown in Fig. 4b. Here three initial conditions in the $(1, 1, 0)$ resonance are iterated only 200 steps and *all* points along the orbits are shown *projected* onto the action-plane. Two of these orbits (red and blue) drift by $\mathcal{O}(1)$ in this small number of iterations, and one (gold) appears to be, at least temporarily, confined near $y_1 = -y_2 \approx -0.3$.

One way to better quantify the drift is to compute the action-diameter of an orbit

$$D(x^{(0)}, y^{(0)}; T) = \max_{0 \leqslant t,s \leqslant T} \|y^{(t)} - y^{(s)}\|. \tag{3.2}$$

A computation of the diameter as a function of initial condition in the action plane is shown in Fig. 5. For the symplectic case, the largest diameters occur at the intersection of the $(1, 1, 1)$ and $(0, 1, 1)$ resonances, where there is overlap-induced chaos. When $\varphi \neq 0$, however, the diameter is nearly an order of magnitude larger almost everywhere in the $(1, 1, 1)$ resonance, except near the rank-two resonance $\omega = (0, 0)$ which is apparently still foliated with invariant tori near the zero-angle plane, recall Fig. 4.

The strong effect of nonzero φ on the dynamics can also be seen by looking at the mean-square displacement of the actions. Figure 6 shows the square of the change in action, $y^{(t)} - y^{(0)}$. For panel (a), the symplectic case, this is averaged over a small ball of initial conditions in the separatrix layer of the $(1, 0, 0)$ resonance, and the y_2 component is shown to have a linearly increasing mean-square

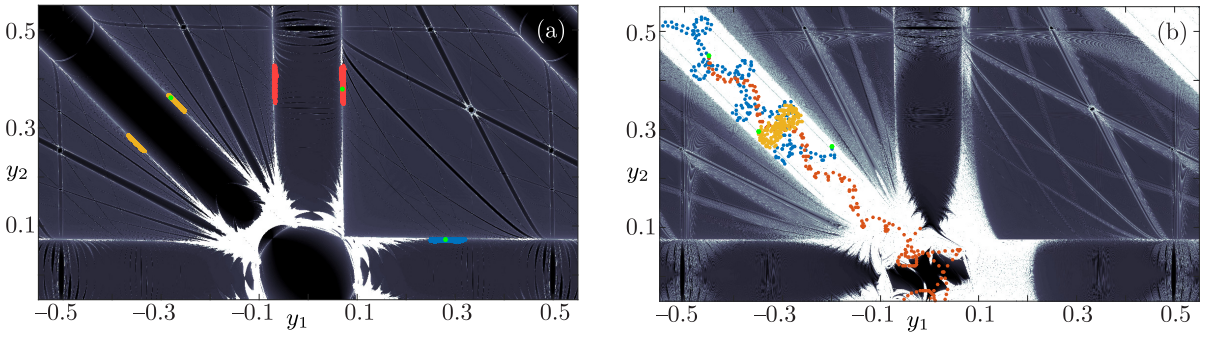

Fig. 4. FLI (grayscale background) for the Froeschlé map with (1.6) and $\varepsilon(a,b,c) = (0.05, 0.05, 0.035)$ on the plane $(0, 0, y_1, y_2)$. Three orbits (color online) are shown in each panel, starting from the small (green) dots. (a) Symplectic ($\varphi = 0$) case with each orbit iterated 10^{10} steps, and only points in a slice near $(x_1, x_2) = 0$ are shown. (b) Volume-preserving ($\varphi = 0.25$) case with each orbit iterated 200 steps, and all points are shown projected onto the action-plane.

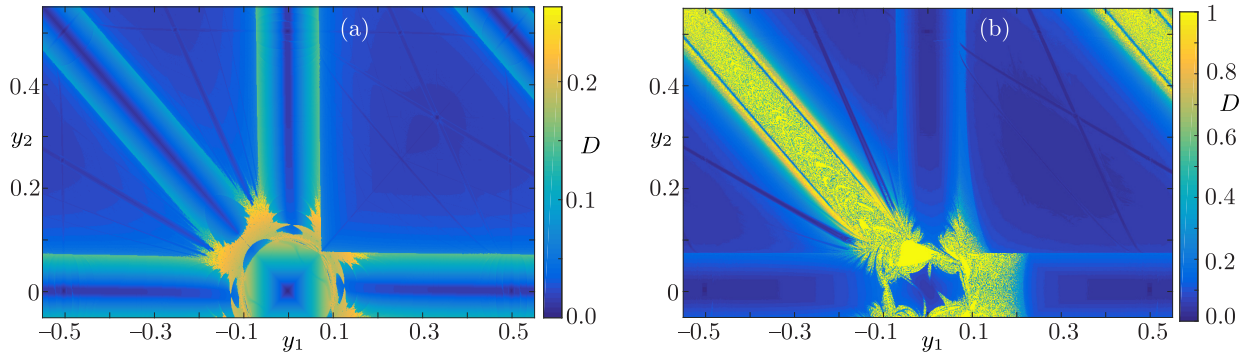

Fig. 5. Orbit diameter (3.2) for initial conditions in the $(0, 0, y_1, y_2)$ plane for (1.2) and (1.6) with $\varepsilon(a,b,c) = (0.05, 0.05, 0.035)$ for $T = 10^3$ iterates. (a) The symplectic case, $\varphi = 0$. (b) The volume-preserving case, $\varphi = 0.25$. Note that the shading scales (color online) are different for the two panels.

drift: the motion is diffusive. By contrast Fig. 6b shows that, for an initial condition in the $(1, 1, 0)$ resonance for the volume-preserving case, the norm of the action has a squared drift that increases as T^2: the motion is ballistic.

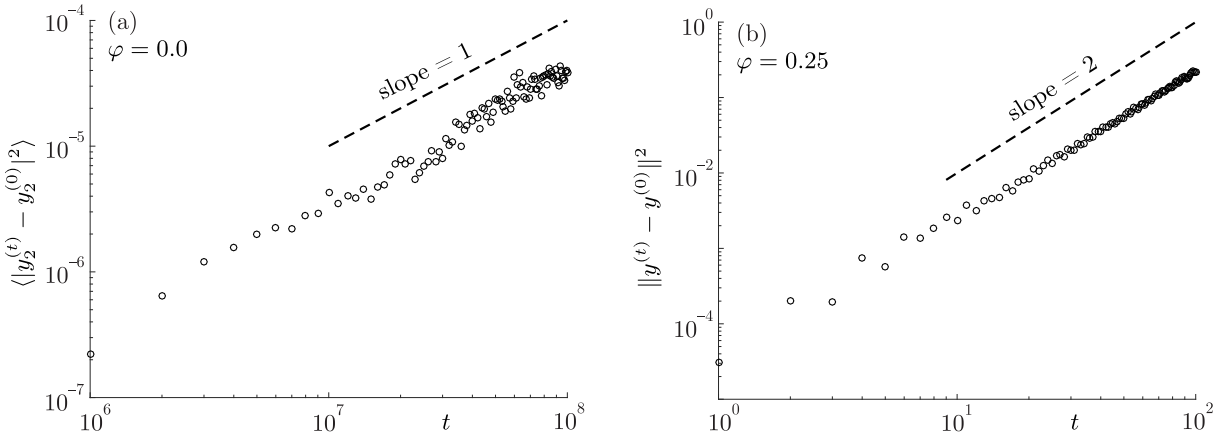

Fig. 6. Growth of the squared action displacement for the same parameters as Fig. 5. (a) Symplectic case. Mean-squared displacement for 100 initial conditions within 10^{-3} of $(0.5, 0, 0, 0.35)$ is still less than 10^{-4} after 10^8 iterations. (b) Volume-preserving case. Squared displacement nears $\mathcal{O}(1)$ for initial condition $(0, 0, -0.45, 0.45)$ after only 100 iterations.

To better understand drift direction we want to compute an approximate action velocity. It is useful to compute a running average by applying *exponential smoothing*. To compute a linear trend for the actions, we use the "Holt – Winters" double exponential smoothing [37], see Appendix C. Figure 7 shows the trend, $V^{(T)}$, from (C.3) in the $(1,-1)$ direction for $T = 100$ on three two-planes of initial conditions. The maximum action drift speeds in this direction are $\approx 5(10)^{-4}$ in the $(1,1,n)$ resonances. This speed is similar to that observed in Fig. 6(b), since there $(\Delta y)^2 \approx 0.25$ after 100 iterates.

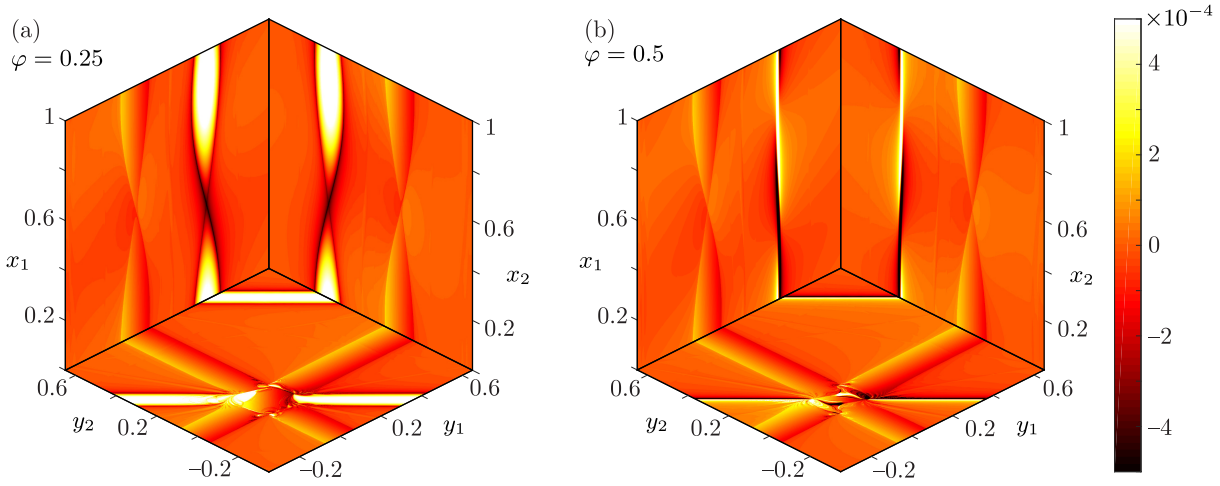

Fig. 7. Smoothed trend planes for the change in action in the $(1,-1)$ direction, for the volume-preserving generalized Froeschlé map for $\varepsilon(a,b,c) = (0.05, 0.05, 0.035)$ for (a) $\varphi = 0.25$ and (b) $\varphi = 0.5$. The shading scale (color online) represents $V^{(T)} \cdot (1,-1)/\sqrt{2}$ for $T = 100$.

4. RESONANT COORDINATES

In this section we will study the drift in the action variables for a map of the form (1.1) for an initial condition in the neighborhood of a point in a rank-r resonance. We will assume that the derivative of the frequency map is symmetric and uniformly positive definite, (2.7).

We will show that, in the correct coordinates, the map can be averaged over the (fast) nonresonant angles to produce an approximate dynamics in semidirect product form. The resonant angle and action variables evolve on this time scale independently of the nonresonant actions. The latter are forced by the resonant dynamics, and we identify the terms that are responsible for causing the drift that we observed in Section 3.

4.1. Resonances

For a rank-r resonance, the module $\mathcal{L}(\omega)$ of (1.4) has a basis $\{m^{(1)}, \ldots, m^{(r)}\} \subset \mathbb{Z}^d$ such that whenever $n_j = m^{(j)} \cdot \omega$, the components of each vector $(m^{(j)}, n_j)$ are coprime (however, the components of a vector $m^{(j)}$ need not be coprime). The resonance module is the range of the $d \times r$ matrix

$$M = \left[m^{(1)}\, m^{(2)}\, \cdots\, m^{(r)} \right]$$

over $\mathbb{Z}$. Every such matrix has a Smith normal form [38],

$$M = PSW, \tag{4.1}$$

with unimodular matrices $P \in Sl(d,\mathbb{Z})$ and $W \in Sl(r,\mathbb{Z})$, and a $d \times r$ diagonal matrix $S = \mathrm{diag}(s_1, \ldots, s_r)$. Here the $s_j \in \mathbb{N}$ have the property that s_j divides s_l for all $j < l$. We will use the transpose of the $d \times d$ matrix P to define new angles, $\xi = P^T x$; the unimodularity of P will preserve

periodicity. Notice that the span of the first r columns of P is $\mathcal{L}(\omega)$, so the first r components of ξ represent the *resonant angles*. The corresponding new frequencies are

$$\hat{\omega} = P^T\omega. \tag{4.2}$$

If we define a vector $n \in \mathbb{Z}^r$ with components n_j, then $n = M^T\omega$, and

$$\hat{n} = W^{-T}n = W^{-T}(W^TS^TP^T)\omega = S^T\hat{\omega} \in \mathbb{Z}^r.$$

Consequently,

$$\hat{\omega} = (\hat{\omega}_S, \hat{\omega}_F) = \left[\frac{\hat{n}_1}{s_1} \ \dots \ \frac{\hat{n}_r}{s_r} \ \hat{\omega}_{r+1} \ \dots \ \hat{\omega}_d\right]^T. \tag{4.3}$$

Since, by assumption, $\dim\big(\mathcal{L}(\omega)\big) = r$, the components of $\hat{\omega}_F$ are incommensurate. We think of $\hat{\omega}_S$ as representing "slow frequencies" and $\hat{\omega}_F$, "fast frequencies".

Given a frequency map $\Omega : \mathbb{R}^d \to \mathbb{R}^d$, and a vector $(m, n) \in \mathbb{Z}^d \times \mathbb{Z}$, the subset

$$\mathcal{R}_{m,n} = \{y \in \mathbb{R}^d : m \cdot \Omega(y) = n\} \tag{4.4}$$

is a *resonance manifold*. Whenever $D\Omega$ is nonsingular, a rank-one resonance is a codimension-one submanifold. Given a point $y_* \in \mathcal{R}_{m,n}$, then a nearby point $y \in \mathcal{R}_{m,n}$ if

$$0 = m \cdot \Omega(y) - n = m \cdot D\Omega_*(y - y_*) + \mathcal{O}(y - y_*)^2,$$

where $D\Omega_* = D\Omega(y_*)$. Therefore, a resonance manifold is locally perpendicular to every vector of the form $D\Omega_*^T m$ for each $m \in \mathcal{L}(\omega)$. A point y_* lies on a rank-r resonance if it is in the intersection of r, independent rank-one resonance manifolds, i. e., if the resonance module (1.4) has dimension r at $\omega = \Omega(y_*)$. This defines a codimension-r submanifold

$$\mathcal{R}_\omega = \bigcap_{m \in \mathcal{L}(\omega)} \mathcal{R}_{m, m\cdot\omega}.$$

When $D\Omega_*$ is symmetric, positive definite, it induces an inner product

$$\langle v, w\rangle_{D\Omega_*} \equiv v^T D\Omega_* w, \tag{4.5}$$

and a corresponding norm $\|\cdot\|_{D\Omega_*}$ This norm can be used to find an orthogonal basis for the module $\mathcal{L}(\omega)$ that will be used to define new action variables[2)]. Applying the Gram – Schmidt process to the columns of P from (4.1) with respect to the inner product (4.5) gives

$$P = QR, \quad Q^T D\Omega_* Q = I, \tag{4.6}$$

where R is upper triangular and Q is orthogonal with respect to (4.5). The first r columns of Q and P have the same span over $\mathbb{R}$ which contains $\mathcal{L}(\omega)$, so the remaining columns of Q are orthogonal to $\mathcal{L}(\omega)$, and therefore span the tangent space to $\mathcal{R}_\omega$ at y_*.

4.2. Expanding and Averaging

For a point $(x, y) \in \mathbb{T}^d \times \mathbb{R}^d$, consider a family of maps f of the form (1.1) where Ω, X, and Y are real analytic, and $D\Omega$ is symmetric and uniformly positive definite, (2.7). Suppose $y_* \in \mathcal{R}_\omega$ for a rank-r rotation vector $\omega = \Omega(y_*)$, and $D\Omega_* \equiv D\Omega(y_*)$. To investigate the possibility of action drift along resonances, we want to define coordinates in a neighborhood y_* that are "natural" to the resonance. First, to balance the size of the perturbing terms we define new action variables δ by

$$y = y_* + \kappa\delta, \text{ where } \kappa \equiv \sqrt{\varepsilon}.$$

[2)] If $D\Omega$ is nonsingular, but not symmetric, we can use the polar decomposition to obtain an appropriate norm, giving essentially the same results.

Expanding (1.1) then gives

$$\begin{aligned} x' &= x + \omega + \kappa D\Omega_* \delta' + \mathcal{O}(\kappa^2) \mod 1, \\ \delta' &= \delta + \kappa Y(x, y_*; 0) + \mathcal{O}(\kappa^2). \end{aligned} \tag{4.7}$$

We then define coordinates (ξ, η) adapted to the resonance using the matrix P from (4.1) and the orthogonal matrix Q from (4.6),[3)]

$$\begin{aligned} \xi &= P^T x, \\ \eta &= Q^{-1}\delta = Q^T D\Omega_* \delta. \end{aligned} \tag{4.8}$$

In the new coordinates the map (4.7) becomes

$$\begin{aligned} \xi' &= \xi + \hat{\omega} + \kappa R^T \eta' + \mathcal{O}(\kappa^2) \mod 1, \\ \eta' &= \eta + \kappa G(\xi) + \mathcal{O}(\kappa^2), \end{aligned} \tag{4.9}$$

where, by (4.2), $\hat{\omega} = P^T\omega$ has the form (4.3), we used (4.6) to obtain

$$P^T D\Omega_* \delta = R^T Q^T D\Omega_* Q\eta = R^T \eta,$$

and we defined the transformed force

$$G(\xi) \equiv Q^{-1} Y(P^{-T}\xi, y_*; 0) = Q^{-1} \sum_{j\in\mathbb{Z}^d} \tilde{Y}_{Pj} e^{2\pi i \xi^T j}, \tag{4.10}$$

which therefore has Fourier coefficients $\tilde{G}_j = Q^{-1}\tilde{Y}_{Pj}$.

The map (4.9) has a natural slow-fast decomposition in terms of the (slow) resonant angles $\xi_S = (\xi_1, \dots \xi_r)^T$ and the (fast) nonresonant angles $\xi_F = (\xi_{r+1}, \dots \xi_d)^T$. Similarly we write the upper triangular matrix R (4.6) in block form as $R = [R_S\, R_F]$. Then since s_r is an integer multiple of each $s_1, s_2, \dots, s_r$, iterating (4.9) $s = s_r$ times to $\mathcal{O}(\kappa^2)$ will eliminate the constant rational frequencies $\hat{n}_j/s_j$ in (4.3). Moreover, since the angles are taken mod 1, we have

$$\begin{aligned} \xi_S^s &= \xi_S^0 + \kappa s R_S^T \eta^s + \mathcal{O}(\kappa^2) \mod 1, \\ \xi_F^s &= \xi_F^0 + s\hat{\omega}_F + \kappa s R_F^T \eta^s + \mathcal{O}(\kappa^2) \mod 1, \\ \eta^s &= \eta^0 + \kappa \sum_{j=0}^{s-1} G(\xi + j\hat{\omega}) + \mathcal{O}(\kappa^2). \end{aligned}$$

If the vector $\hat{\omega}_F$ is Diophantine, the averaging results of [11, see §5] imply that the fast angles ξ_F can be averaged away on the time scale $\mathcal{O}(\kappa^{-1}) \gg 1$, leaving

$$\begin{aligned} \xi_S^s &= \xi_S^0 + \kappa s R_S^T \eta^s + \mathcal{O}(\kappa^2) \mod 1, \\ \eta^s &= \eta^0 + \kappa s \bar{G}(\xi_S^0) + \mathcal{O}(\kappa^2), \end{aligned} \tag{4.11}$$

where the resonant force is

$$\begin{aligned} \bar{G}(\xi_S) &= \frac{1}{s}\int_{\mathbb{T}^{d-r}} \sum_{j=0}^{s-1} G(\xi + j\hat{\omega})\, d\xi_F = \frac{1}{s}\sum_{j=0}^{s-1}\sum_{l\in\mathbb{Z}^d} \tilde{G}_l e^{2\pi i j\hat{\omega}\cdot l} \int_{\mathbb{T}^{d-r}} e^{2\pi i \xi\cdot l}\, d\xi_F \\ &= \sum_{l_S\in\mathbb{Z}^r} \tilde{G}_{(l_S,0)} e^{2\pi i \xi_S\cdot l_S} \frac{1}{s}\sum_{j=0}^{s-1} e^{2\pi i j\hat{\omega}_S\cdot l_S} = \sum_{l_S\in\mathcal{L}(\hat{\omega}_S)} \tilde{G}_{(l_S,0)} e^{2\pi i \xi_S\cdot l_S}, \end{aligned} \tag{4.12}$$

[3)] This transformation is not canonically symplectic unless by chance $Q = P$, i. e., P is $D\Omega_*$ orthogonal. For a general frequency map, the transformation is also not volume-preserving, but has constant Jacobian, $\det(Q)^{-1}$. Thus, when f preserves volume, so will the map in the new coordinates.

and $\mathcal{L}(\hat{\omega}_S) = \{l_S \in \mathbb{Z}^r : \hat{\omega}_S \cdot l_S \in \mathbb{Z}\}$ is the r-dimensional resonance lattice for the slow, resonant frequencies. In [11] it was shown that this averaging transformation can be repeated to n^{th} order in such a way that the orbit of the averaged system for the slow variables is within $\mathcal{O}(\kappa^{-n})$ of the slow projection of the true system for times up to $\mathcal{O}(\kappa^{-1})$. Moreover, if the map is volume-preserving (symplectic), one can choose the transformation to also be volume-preserving (symplectic).

Since R is upper triangular, the averaged map (4.11) has the form of a semidirect product: the dynamics of (ξ_S, η_S) do not depend on the nonresonant action variables, η_F, up to $\mathcal{O}(\kappa^2)$.

If the map (1.1) were canonically symplectic in the original variables (x, y), these actions (locally aligned with the resonance) are fixed, up to $\mathcal{O}(\kappa^2)$: indeed, whenever the force $Y(x, y_*, 0)$ is a gradient, its Fourier coefficients satisfy $\tilde{Y}_l \propto l$ so that, from (4.10),

$$\tilde{G}_{(l_S,0)} \propto Q^{-1} P \begin{bmatrix} l_S \\ 0 \end{bmatrix} = R \begin{bmatrix} l_S \\ 0 \end{bmatrix} = R_S l_S$$

is always zero in the bottom $d - r$ components (again since R is upper triangular). Of course, for this case, when $D\Omega_*$ is symmetric and positive definite, Theorem 1 implies much more: that the drift in all the actions is small for exponentially long times. On the other hand, if the force is not a gradient, then the nonresonant actions in (4.11) can experience forces that depend upon the slow angles ξ_S and have a nonzero average, leading to large drifts.

5. ACTION DRIFT IN RANK-ONE RESONANCES

For a rank-one resonance, the averaged force (4.12) depends upon a single angle, $\xi_1 \propto m \cdot x$, and the averaged system (4.11) reduces to

$$\begin{aligned} \xi_1^s &= \xi_1^0 + \kappa \|m\|_{D\Omega_*} \eta_1^s + \mathcal{O}(\kappa^2) \mod 1, \\ \eta^s &= \eta^0 + \kappa s \bar{G}(\xi_1^0) + \mathcal{O}(\kappa^2), \end{aligned} \tag{5.1}$$

since, when $r = 1$, we know

$$sR_{11} = s\|p^{(1)}\|_{D\Omega_*} = \|m\|_{D\Omega_*},$$

where $p^{(1)}$ is the first column of P in (4.1).

The first two components of (5.1) are a generalized Chirikov area-preserving map. These components reduce to the standard map when $\bar{G}$ has only a single Fourier component $l = \pm s$:

$$\bar{G}(\xi_1) = \tilde{G}_{(s,0)} e^{2\pi i s \xi_1} + \tilde{G}_{(-s,0)} e^{-2\pi i s \xi_1} = Q^T D\Omega_* (\tilde{Y}_m e^{2\pi i s \xi_1} + \tilde{Y}_{-m} e^{-2\pi i s \xi_1}),$$

so that $\bar{G}_1(\xi_1) = \frac{a_1}{2\pi} \cos(2\pi s \xi_1 + \theta)$, where

$$a_1 = \frac{4\pi}{\|m\|_{D\Omega_*}} \left| m^T D\Omega_* \tilde{Y}_m \right| \qquad \text{and} \qquad \theta = \arg(m^T D\Omega_* \tilde{Y}_m),$$

since $q^{(1)} = m/\|m\|_{D\Omega_*}$. When a_1 is small, the dynamics of this map are dominated by the resonance island near $\eta_1 = 0$, recall Fig. 1. The half-width of this island is

$$\Delta\eta_1 = \frac{1}{\pi} \sqrt{\frac{a_1}{\|m\|_{D\Omega_*}}},$$

but $\Delta\eta_1 = \frac{1}{\kappa \|m\|_{D\Omega_*}} m^T D\Omega_* \Delta y$, so the half-width with respect to y in the $D\Omega_* m$ direction (locally perpendicular to the resonance) is

$$w_m = \frac{2}{\|D\Omega_* m\|} \sqrt{\frac{\varepsilon}{\pi} \left| m^T D\Omega_* \tilde{Y}_m \right|}.$$

Note that the nonresonant actions in (5.1) are forced by the resonant angle ξ_1 through $\bar{G}_j(\xi_1)$, $j = 2, \ldots, d$. The components of this force that are out-of-phase with $\bar{G}_1(\xi_1)$ are responsible for the

drift. To see this, consider the special case that the first component of $\bar{G}$ is a pure sine function (e. g., $\theta \to \pi/2$), and that $s = \|p^{(1)}\| = 1$. Then, upon setting the formal parameter $\kappa \to 1$, the averaged dynamics of (5.1) become the $(1+d)$-dimensional slow map

$$\begin{aligned} \xi_1' &= \xi_1 + \eta_1' \mod 1, \\ \eta_1' &= \eta_1 - \frac{a_1}{2\pi}\sin(2\pi\xi_1), \\ \eta_j' &= \eta_j - \frac{1}{2\pi}\big(a_j \sin(2\pi\xi_1) + b_j \cos(2\pi\xi_1)\big), \quad j = 2, \dots, d. \end{aligned} \tag{5.2}$$

The standard map dynamics in (ξ_1, η_1) then provides a oscillatory force on the remaining (drifting) actions, $\eta_2, \cdots, \eta_d$. If $a_1 \neq 0$, then after T iterations

$$\eta_j^{(T)} - \eta_j^{(0)} = -\frac{1}{2\pi}\sum_{t=0}^{T-1} a_j \sin\left(2\pi\xi_1^{(t)}\right) + b_j \cos\left(2\pi\xi_1^{(t)}\right) = \frac{a_j}{a_1}\left(\eta_1^{(T)} - \eta_1^0\right) - \frac{T}{2\pi} b_j \langle \cos(2\pi\xi_1)\rangle_T,$$

where

$$\langle \cos(2\pi\xi_1)\rangle_T = \frac{1}{T}\sum_{t=0}^{T-1} \cos\left(2\pi\xi_1^{(t)}\right) \tag{5.3}$$

is the time average along the standard map orbit. When $|a_1| \lesssim 0.971$, the critical parameter for the destruction of the last rotational invariant circle of the standard map, the resonant action η_1 is bounded. Thus, when $T \gg 1$ we have

$$\frac{\eta^{(T)} - \eta^{(0)}}{T} \approx -\frac{b}{2\pi}\langle \cos(2\pi\xi_1)\rangle_T. \tag{5.4}$$

Note that the long term drift is parallel to b, the vector of amplitudes of the out-of-phase forcing of the drift actions. For $T \gg 1$, $\langle \cos(2\pi\xi_1)\rangle_T$ will limit to a constant value determined by the decoupled standard map orbit. An example is shown in Fig. 8 for the case $a_1 = 0.52$. Note that inside the fixed point resonance there is a domain for which $|\xi_1^{(t)}|$ is small for all t, and thus $\cos(2\pi\xi_1^{(t)}) > 0$, resulting in a positive time average. By contrast, orbits near the separatrix of the resonance spend a majority of their time near the saddle fixed point at $(0.5, 0)$, giving a negative average. Between these extremes there is a tube where $\langle \cos(2\pi\xi_1)\rangle_T \approx 0$. We will refer to this as *bidirectional drift* in contrast to the unidirectional drift that would be caused by a constant forcing term. We saw bidirectional drift in Fig. 4b — the different behavior of three orbits shown corresponds to the variation in direction as one changes the diameter of the resonant dynamics.

Thus, in addition to the (symplectic) case where $a_j = b_j = 0$ for $j \geqslant 2$, in order to prevent drift — to lowest order — it is sufficient that $b = 0$, i. e., that all drift action forcing is in phase with the resonant action forcing. One can also study higher-order terms in the expansion about a resonance to understand the change in direction of the drift as the action changes [39].

6. DRIFT IN THE GENERALIZED FROESCHLÉ MAP

As the simplest example, we return to the generalized Froeschlé map (1.2) on $\mathbb{T}^2 \times \mathbb{R}^2$, with force and frequency map (1.6). The amplitudes a, b, and c create the $(1, 0, n)$, $(0, 1, n)$ and $(1, 1, n)$ resonances, respectively.

Suppose first that y_* is a point in an $(1, 1, n)$ resonance, so that $y_{1*} + y_{2*} = n$. Since $D\Omega = I$, the transformation matrices in (4.6) become

$$P = \begin{pmatrix} 1 & 1 \\ 1 & 2 \end{pmatrix} = QR = \frac{1}{\sqrt{2}}\begin{pmatrix} 1 & -1 \\ 1 & 1 \end{pmatrix}\begin{pmatrix} \sqrt{2} & 3/\sqrt{2} \\ 0 & 1/\sqrt{2} \end{pmatrix},$$

so that the new variables of (4.8) are

$$(\xi_1, \xi_2) = (x_1 + x_2, x_1 + 2x_2),$$

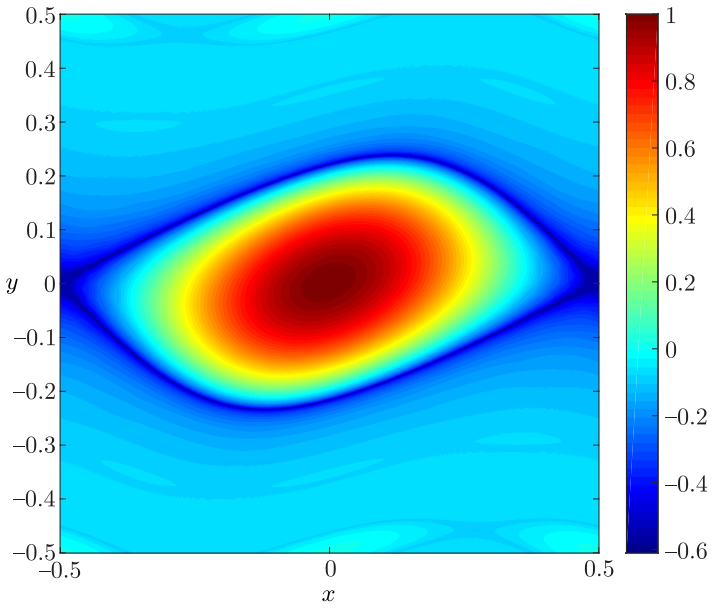

Fig. 8. Time average of $\cos(2\pi\xi_1)$, (5.3), for orbits of the standard map for $a_1 = 0.52$, with 10^6 initial conditions on a square grid, each iterated 10^3 steps

$$(\eta_1, \eta_2) = \tfrac{1}{\sqrt{2}\kappa}(y_1 + y_2 - n, y_2 - y_1 + y_{1*} - y_{2*}),$$

and the new frequency, (4.2), is $\hat{\omega} = (\omega_S, \omega_F) = (n, y_{1*} + 2y_{2*})$. By periodicity and the resonance condition, the constant frequency for angle ξ_1 vanishes mod 1, so the transformed map, (4.9), becomes

$$\begin{aligned}
\xi_1' &= \xi_1 + \kappa\sqrt{2}\eta_1' \mod 1 \\
\xi_2' &= \xi_2 + \omega_F + \mathcal{O}(\kappa) \mod 1 \\
\eta' &= \eta - \kappa\frac{c}{\sqrt{2}\pi}\begin{bmatrix} \cos(\pi\varphi)\sin\big(2\pi(\xi_1 + \varphi/2)\big) \\ \sin(\pi\varphi)\cos\big(2\pi(\xi_1 + \varphi/2)\big) \end{bmatrix} + \mathcal{O}(\kappa a, \kappa b).
\end{aligned}$$

If the second frequency ω_F is Diophantine, then for κ small enough we can apply the averaging procedures to push the ξ_2 dependence in the a, b forcing terms to $\mathcal{O}(\kappa^2)$. Defining a final shifted angle $\xi_1 = \xi_1 + \varphi/2$, at first order we then obtain a slow map of the form (5.2) with

$$a_1 \propto c\cos(\pi\varphi), \qquad a_2 = 0, \qquad b_2 \propto c\sin(\pi\varphi)$$

which has orbits that are conjugate to $\mathcal{O}(\kappa^2)$ to the projection of an orbit of the original map onto the slow variables for times $\mathcal{O}(\kappa^{-1})$. The drift in η_2 vanishes for the symplectic case $\varphi = 0$, but otherwise $b_2 \neq 0$. The result is bidirectional drift in $(1, 1)$ resonances, as discussed in Section 5.

A comparison of the theory with computations is given in Fig. 9. To do this, we compute the exact dynamics for an orbit that starts near the elliptic point of the (ξ_1, η_1) dynamics in the $(1, 1, 0)$ resonance. Thus, we set $(x, y) = \Big(-\frac{1}{2}\varphi, 0, -0.35, 0.35\Big)$ when $0 \leqslant \varphi < \frac{1}{2}$ and $(x, y) = \Big(\frac{1}{2}(1 - \varphi), 0, -0.35, 0.35\Big)$ when $\frac{1}{2} < \varphi \leqslant 1$ since the sign of a_1 changes at $\varphi = \frac{1}{2}$, where the amplitude of the resonance vanishes to $\mathcal{O}(\kappa)$. After iterating 10^3 steps we compute a linear fit to the values of $\eta_2^{(t)}$ to obtain the slope; this gives the drift shown in the figure as a function of φ. The numerical points agree very well with the theoretical drift from (5.4), also shown — except for a small deviation near the discontinuity at $\varphi = \frac{1}{2}$.

Consider now a point y_* in an $(1, 0, n)$ resonance, $m \cdot \Omega(y_*) = y_{1*} = n$, where Ω is the identity map. Since $\xi_1 = m \cdot x = x_1$, the map (1.2) is already written in resonant coordinates, once we define

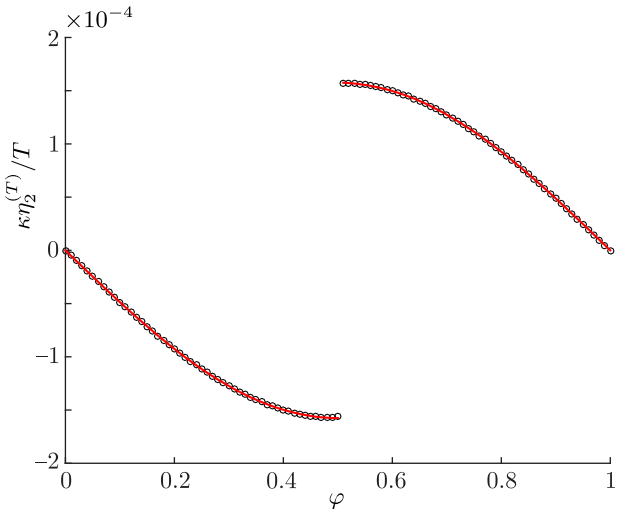

Fig. 9. Comparison of the computed drift in $\kappa\eta_2^{(t)}$ to the analytical drift from (5.4) in the $(1,1,0)$ resonance with actions $y^{(0)} = (-0.35, 0.35)$ iterated $T = 10^3$ steps, for the generalized Froeschlé map with $\varepsilon(a,b,c) = (0.001, 0.001, 0.0007)$. The curve (red) shows the analytical drift $-\kappa^2 \frac{c}{\sqrt{2}\pi} \sin(\pi\varphi) \operatorname{sgn}\big(\cos(\pi\varphi)\big)$ from (5.4).

$\delta = (y - y_*)/\kappa$:

$$
\begin{aligned}
x_1' &= x_1 + \kappa\delta_1' \mod 1,\\
x_2' &= x_2 + \omega_F + \mathcal{O}(\kappa) \mod 1,\\
\delta' &= \delta - \frac{\kappa}{2\pi}\begin{bmatrix} a\sin(2\pi x_1) \\ 0 \end{bmatrix} + \mathcal{O}(\kappa b, \kappa c).
\end{aligned}
$$

Here the fast frequency is $\omega_F = y_{2*}$ and, since this is almost always irrational, the resonance has rank one. Under first-order averaging, the fast x_2 dependence in the b, c forcing terms is zero to $\mathcal{O}(\kappa^2)$, so that δ_2 is conserved to $\mathcal{O}(\kappa^2)$ on the time scale $t \sim \mathcal{O}(\kappa^{-1})$. However, we can carry out the averaging procedure to two more orders to remove the fast dependence up to $\mathcal{O}(\kappa^4)$ and compute a nonzero drift. This procedure gives

$$
\begin{aligned}
\xi_1' &= \xi_1 + \kappa\eta_1' \mod 1,\\
\eta_1' &= \eta_1 - \frac{1}{2\pi}\left(\kappa a - \kappa^3 \frac{bc}{8\sin^2(\pi\omega_F)}\right)\sin(2\pi\xi_1) - \kappa^3 \frac{c^2}{16\pi\sin^2(\pi\omega_F)}\sin(2\pi\varphi),\\
\eta_2' &= \eta_2 + \kappa^3 \frac{c^2}{16\pi\sin^2(\pi\omega_F)}\ \sin(2\pi\varphi).
\end{aligned}
\tag{6.1}
$$

Note that in this case the drift term in η_2 is independent of the slow variables. For $\varphi \neq 0$ or $\frac{1}{2}$, this implies unidirectional drift in $(1,0,n)$ resonances that is second order in ε with respect to the original variables. The drift speed depends on ω_F and is nonzero and finite except at a double resonance when $\omega_F \in \mathbb{Z}$. By symmetry, a similar second order drift exists for orbits in $(0,1,n)$ resonances as well.

We show a comparison of this second order drift with computations in Fig. 10. Panel (a) shows the variation in drift with φ, and (b) with ω_F. Again the analysis agrees with the numerical computations, though there is a visible deviation between the theory and computations as a function of the phase shift.

7. CONCLUSIONS

Action-angle maps, like (1.1), are natural as descriptions of the dynamics of nearly integrable systems. When such a map is symplectic and has a positive-definite twist, it has a strong

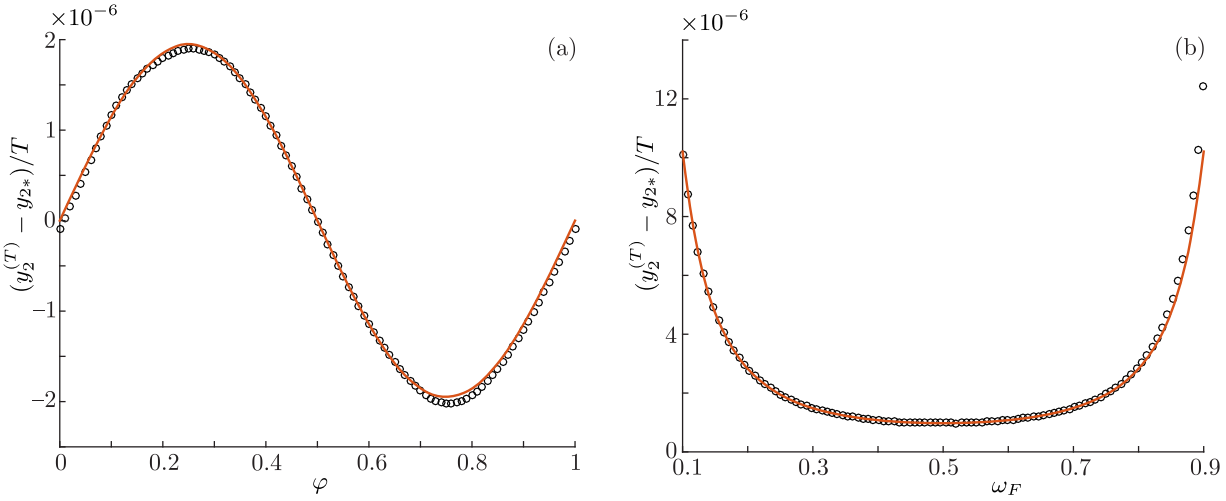

Fig. 10. Comparison of the drift in $y_2^{(t)} - y_{2*}$ to the analytical drift from the third-order averaged map (6.1) for an orbit of length $T = 10^3$, starting at $(x, y) = (0, 0, 0, y_{2*})$ in the $(1, 0, 0)$ resonance of the generalized Froeschlé map with (1.6). Here $\varepsilon(a, b, c) = (0.01, 0.01, 0.007)$. (a) Variation of the drift with φ when $\omega_F = y_{2*} = 0.25$. (b) Variation of the drift as a function of $\omega_F = y_{2*}$ when $\varphi = 0.25$. The curves show the analytical drift $\kappa^4 c^2 \sin(2\pi\varphi)/\big(16\pi \sin^2(\pi\omega_F)\big)$.

quasi-stability property due to Nekhoroshev's theorem: for $\varepsilon \ll 1$ the actions are confined for exponentially long times. By contrast, when the map is merely volume-preserving, we showed that the actions can drift along resonances much more rapidly than the exponentially slow diffusion of a symplectic map. This is due to the simple geometrical fact that when the symplectic condition is relaxed the resonant forces are no longer orthogonal to the resonance manifold $m \cdot \Omega(y) = n$. The average dynamics show that the drift speed along the resonance has a sign that depends on whether the resonant subsystem is trapped in the elliptic island or is in the chaotic separatrix region of the resonance; the drift is "bidirectional".

For the generalized Froeschlé map (1.2) that we studied in this paper, with the simple force $F(x)$ and frequency map $\Omega(y)$ (1.6), the nonsymplectic term is — to lowest order — only important in $(m, n) = (1, 1, n)$ resonances since the nonsymplectic coupling term is slowly varying in these resonances. Of course, to higher order, as noted in Section 6, nonlinearity of the map can also cause drift in other resonances.

It is interesting, however, to consider the effect of more general forces. For example, the force

$$F_{fs} = -\frac{1}{2\pi} \frac{d}{\big(2.1 + \cos(2\pi x_1) + \cos(2\pi x_2)\big)^2} \begin{pmatrix} \sin(2\pi x_1) \\ \sin\big(2\pi(x_2 + \varphi_{fs})\big) \end{pmatrix} \tag{7.1}$$

has been studied in [22] for the symplectic case $\varphi_{fs} = 0$, where it is a gradient. This force has a full spectrum of Fourier coefficients. When $\varphi = \varphi_{fs} = 0$, the drift of the actions in a map with force $F(x) + F_{fs}(x)$ is still constrained by Nekhoroshev's theorem since the map is symplectic and the twist is positive definite. Figure 11 shows the FLI (in grayscale as in Fig. 4) on the plane $x = (0, 0.25)$. Note that there are many more (small) resonance channels visible in this FLI plot than there were for the force (1.6) alone. Also shown in the figure are points on seven clusters of orbits, each started near the small black dots in the figure. Each of these clusters consist of the 100 orbits that have the largest FLI values in the neighborhood of the initial point. The orbits are iterated 10^8 times, but points are plotted only when they fall within 10^{-3} of the plane. Note that the drift in actions for each of these clusters is small: the total change is less than $\mathcal{O}(0.1)$.

By contrast, when φ or $\varphi_{fs} \neq 0$, the drift can be large, even in narrow resonance channels. An example is shown in Fig. 12 for a map with the same parameters as that in Fig. 11 except that $\varphi_{fs} = 0.5$. The FLI for this volume-preserving system is hard to distinguish from the symplectic case. However, the points on the single cluster of orbits shown now exhibit drifts with size $\mathcal{O}(1)$ in

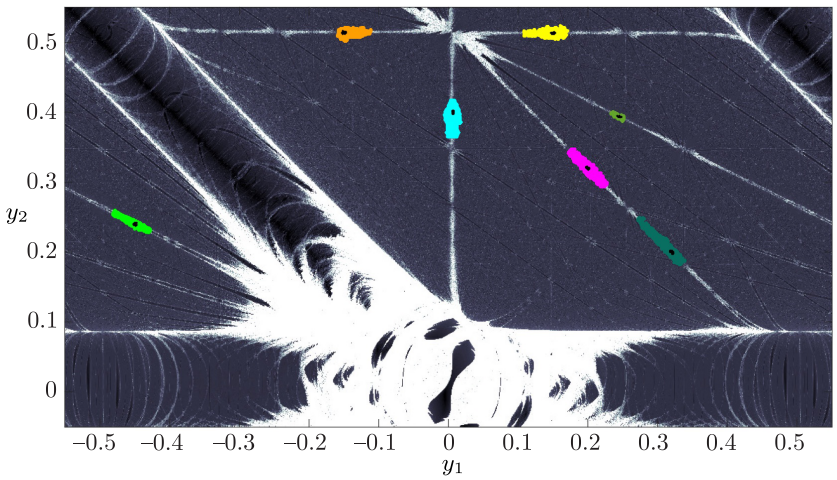

Fig. 11. Drift in the symplectic generalized Froeschlé map with (1.6) and parameters $(a, b, c) = (0, 0.1, 0.07)$, $\varphi = 0.0$ as well as an added full spectrum force (7.1) with $d = 10^{-4}$ with $\varphi_{fs} = 0.0$. The grayscale shows the FLI for initial conditions in the plane $(0, 0.25, y_1, y_2)$. Also shown are the points on seven clusters of orbits of length $T = 10^8$ that have the largest values of the FLI near the initial value (black dots). Each cluster is 100 orbits, and points are shown only if they are within 10^{-3} of the slice.

10^8 steps. Note also that the drifting orbit moves from one rank-one resonance channel to another when it reaches a rank-two crossing. We plan to investigate these transitions in a future paper.

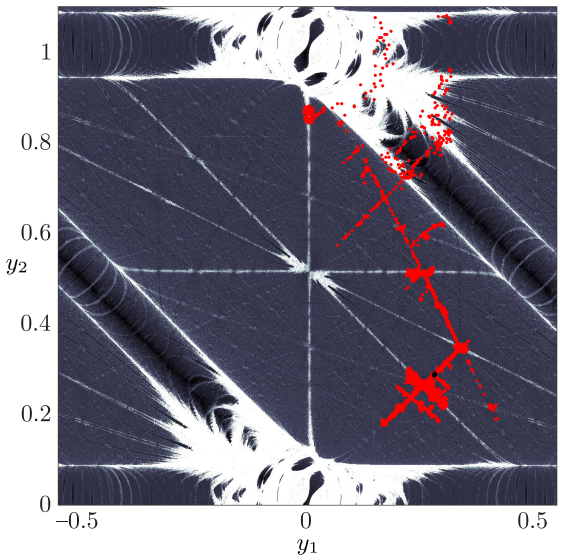

Fig. 12. Drift in a volume-preserving, full-spectrum, generalized Froeschlé map with the same parameters as Fig. 11 except that $\varphi_{fs} = 0.5$. The grayscale shows the FLI for initial conditions in the plane $(0, 0.5, y_1, y_2)$. Also shown are the points (red online) on a cluster of 100 orbits of length $T = 10^8$ that have the largest FLI values near the initial point $(x, y) = (0, 0.5, 0.28, 0.288)$ (black dot).

APPENDIX A. REVERSIBILITY

An invertible map f is *reversible* if there exists an involution S ($S^2 = I$) such that

$$S \circ f = f^{-1} \circ S. \tag{A.1}$$

The map S is called a *reversing symmetry* for f [40]. The generalized Froeschlé map (1.2) for any d and k is reversible whenever the force is odd, $F(-x) = -F(x)$, under the reversor

$$S_1 : \begin{cases} x' &= -x, \\ y' &= y + \varepsilon F(x). \end{cases}$$

Similarly, if the frequency map is odd, $\Omega(-y) = -\Omega(y)$, f has the reversor

$$S_2 : \begin{cases} x' &= x, \\ y' &= -y - \varepsilon F(x). \end{cases}$$

These reversors can be generalized to functions that are odd about another point, besides the origin [41].

The composition of a symmetry and a reversor is a reversor, and the collection of symmetries and reversors forms the "reversing symmetry group". The map f has two obvious symmetries. First f is a symmetry of itself; so, if S is a reversor, so is $f^t \circ S$, for any $t \in \mathbb{Z}$. The second symmetry is induced by the rotation $R_m(x, y) = (x + m, y)$ for any $m \in \mathbb{Z}$. If we lift f to $\mathbb{R}^{d+k}$, then $f \circ R_m = R_m \circ f$. This implies that $S \circ R_m$ is a reversor.

A periodic orbit is "symmetric" if it is invariant under a reversor S. In such a case the orbit necessarily has points on either fixed set $\mathrm{Fix}(S) = \{(x, y) : S(x, y) = (x, y)\}$ or $\mathrm{Fix}(f \circ S)$ [42]. For example, the fixed sets of the S_1 reversor are d-manifolds $\mathrm{Fix}(S_1) = \{x = 0\}$ and $\mathrm{Fix}(f \circ S_1) = \{\Omega(y) = 2x\}$. The rotation gives additional reversors with the fixed sets $\mathrm{Fix}(S_1 \circ R_m) = \{x = \frac{1}{2}m\}$ and $\mathrm{Fix}(f \circ S_1 \circ R_m) = \{\Omega(y) = 2x - m\}$ that are helpful in classifying the periodic orbits.

APPENDIX B. STABILITY AND REFLEXIVITY

Recall that linear stability is determined by the eigenvalues of the product of the Jacobians $Df(x^{(t)}, y^{(t)})$ evaluated along the orbit. For the generalized Froeschlé map (1.2), the Jacobian is (2.3). We call these eigenvalues the "multipliers" of the orbit.

An important property of symplectic maps with a constant Poisson matrix (like J in (2.2)) is that the multipliers of any periodic orbit have the reflexive property: whenever λ is an eigenvalue, then λ^{-1} is also an eigenvalue with the same multiplicity. This follows from the symplectic condition (2.2), which upon differentiation gives

$$JDfJ^{-1} = Df^{-T}.$$

Thus, Df is conjugate to its inverse transpose, implying that Df and Df^{-1} have the same characteristic polynomials.

Reflexivity holds also for symmetric orbits of reversible maps. Differentiation of the conjugacy (A.1) between f and f^{-1} gives

$$DS\big(f(z)\big)Df(z) = Df^{-1}\big(S(z)\big)DS(z),$$

so that if $z = (x_*, y_*)$ is a fixed point of both f and S, then Df is conjugate to Df^{-1}. Note that the linearization of the generalized Froeschlé map (1.2) about a fixed point is reversible for *any* dimensions d and k and *any* force and frequency map (even if the map itself is not globally reversible). Indeed, the linearization is the map

$$\delta x' = x + D\Omega(y_*)\delta y',$$
$$\delta y' = y + \varepsilon DF(x_*)\delta x,$$

which has the same form as (1.2) with the odd force $DF\delta x \to F(\delta x)$ and odd frequency map $D\Omega\delta y \to \Omega(\delta y)$. Thus, by the results of Appendix A, this map is reversible with, e. g., the linear reversor $S_1(\delta x, \delta y) = (-\delta x, \delta y + \varepsilon DF\delta x)$. Consequently, the eigenvalues of the matrix (2.3) have the reflexive property at any point (x, y).

For example, for $d = k = 2$, the characteristic polynomial for (2.3) at a fixed point is

$$\begin{aligned} p(\lambda) &= \det(Df - \lambda I) = \lambda^4 - A\lambda^3 + B\lambda^2 - A\lambda + 1, \\ A &= \operatorname{tr}(Df) = 4 + \operatorname{tr}(D\Omega DF) \\ B &= \tfrac{1}{2}\big[\operatorname{tr}(Df)^2 - \operatorname{tr}(Df^2)\big] = 6 + 2\operatorname{tr}(D\Omega DF) + \det(DF)\det(D\Omega). \end{aligned} \tag{B.1}$$

Since the coefficients of λ^3 and λ are the same in the characteristic polynomial, whenever $p(\lambda) = 0$ then $p(\lambda^{-1}) = 0$ too. Therefore we cannot distinguish the properties of the generalized map (1.2) from the symplectic case on the basis of eigenvalues of its fixed points alone.

However, it is easy to see by example that when DF or $D\Omega$ is not symmetric, the reflexive property does not generally hold for orbits with period larger than one. The implication is that in this case the map (1.2) cannot be symplectic with a constant Poisson matrix.

APPENDIX C. SMOOTHING

To compute the drift of action, we use exponential smoothing. Given a sequence $\{z^{(t)} : t = 0, 1, \ldots\}$, we define

$$\langle z\rangle_\lambda^t \equiv N \sum_{s=0}^{t} z^{(t-s)} e^{-\lambda s}, \quad N = 1 - e^{-\lambda}. \tag{C.1}$$

Here the normalization factor N is appropriate when $t \gg \lambda^{-1}$, since

$$\langle 1\rangle_\lambda^t = 1 - e^{-\lambda(t+1)} \quad \xrightarrow[t\to\infty]{} \quad 1.$$

This process gives the majority of the weight for the average to the most recent data; for instance, if $\lambda = 0.01$, then the most recent 100, 200, and 300 iterates are given $63\%, 86\%$, and 95% of the weight, respectively. The smoothing (C.1) can be easily computed iteratively by

$$\langle z\rangle_\lambda^t = N z^{(t)} + (1 - N)\langle z\rangle_\lambda^{t-1}, \quad \langle z\rangle_\lambda^{-1} \equiv 0. \tag{C.2}$$

For example, applying this to the changes in the lifted angle $z^{(t)} = x^{(t+1)} - x^{(t)}$ gives a running average of the rotation vector $\omega^{(t)}$. When Ω is the identity map in (1.2) $x^{(t+1)} - x^{(t)} = y^{(t)}$, so this is equivalent to a smoothed action $J^{(t)} = \langle y\rangle_\lambda^t$.

For maps with drifting orbits, we want to obtain a linear trend for the actions. This can be done with the "Holt-Winters" double exponential smoothing [37] which computes two smoothed variables, a mean $J^{(t)}$ and a trend $V^{(t)}$, using the iteration

$$\begin{aligned} J^{(t)} &= N_1 y^{(t)} + (1 - N_1)\big(J^{(t-1)} + V^{(t-1)}\big) \\ V^{(t)} &= N_2\big(J^{(t)} - J^{(t-1)}\big) + (1 - N_2)V^{(t-1)}, \end{aligned} \tag{C.3}$$

where $N_i = 1 - e^{-\lambda_i}$ for exponents λ_1 and λ_2. Here one typically takes $J^{(1)} = y^{(1)}$, and $V^{(1)} = y^{(1)} - y^{(0)}$. The forecasted trend at time t is given by $\langle y\rangle^{t+s} = J^{(t)} + sV^{(t)}$.

For our computations we typically set $\lambda_1 = \lambda_2 = 0.01$.

ACKNOWLEDGMENTS

The authors were supported in part by NSF grant DMS-1211350. We thank A. Bäcker, R. Easton, and R. Ketzmerick for helpful conversations, and J. Laskar for posing an interesting question.

REFERENCES

1. Arnold, V. I., On the Nonstability of Dynamical Systems with Many Degrees of Freedom, *Soviet Math. Dokl.,* 1964, vol. 5, no. 3, pp. 581–585; see also: *Dokl. Akad. Nauk SSSR,* 1964, vol. 156, no. 1, pp. 9–12.
2. Arnold, V. I., Small Denominators and Problems of Stability of Motion in Classical and Celestial Mechanics, *Russian Math. Surveys,* 1963, vol. 18, no. 6, pp. 85–191; see also: *Uspekhi Mat. Nauk,* 1963, vol. 18, no. 6(114), pp. 91–192.
3. Pöschel, J., A Lecture on the Classical KAM Theorem, in *Smooth Ergodic Theory and Its Applications (Seattle, Wash., 1999),* Proc. Sympos. Pure Math., vol. 69, Providence, R.I.: AMS, 2001, pp. 707–732.
4. de la Llave, R., A Tutorial on KAM Theory, in *Smooth Ergodic Theory and Its Applications (Seattle, Wash., 1999),* Proc. Sympos. Pure Math., vol. 69, Providence, R.I.: AMS, 2001, pp. 175–292.
5. Nekhoroshev, N. N., An Exponential Estimate of the time of Stability of Nearly Integrable Hamiltonian Systems, *Russian Math. Surveys,* 1977, vol. 32, no. 6, pp. 1–65; see also: *Uspekhi Mat. Nauk,* 1977, vol. 32, no. 6(198), pp. 5–66, 287.
6. Lochak, P., Canonical Perturbation Theory via Simultaneous Approximations, *Russian Math. Surveys,* 1992, vol. 47, no. 6, pp. 57–133; see also: *Uspekhi Mat. Nauk,* 1992, vol. 47, no. 6(288), pp. 59–140.
7. Arnold, V., Sur la topologie des écoulements stationnaires des fluides parfaits, *C. R. Acad. Sci. Paris,* 1965, vol. 261, pp. 17–20.
8. Cartwright, J. H. E., Feingold, M., and Piro, O., Passive Scalars and Three-Dimensional Liouvillian Maps, *Phys. D,* 1994, vol. 76, nos. 1–3, pp. 22–33.
9. Chirikov, B., A Universal Instability of Many-Dimensional Oscillator Systems, *Phys. Rep.,* 1979, vol. 52, no. 5, pp. 263–379.
10. Froeschlé, C., Numerical Study of a Four-Dimensional Mapping, *Astronom. and Astrophys.,* 1972, vol. 16, pp. 172–189.
11. Dullin, H. R. and Meiss, J. D., Resonances and Twist in Volume-Preserving Mappings, *SIAM J. Appl. Dyn. Syst.,* 2012, vol. 11, no. 1, pp. 319–349.
12. Cheng, Ch. Q. and Sun, Y. S., Existence of Invariant Tori in Three-Dimensional Measure-Preserving Mappings, *Celestial Mech. Dynam. Astronom.,* 1989/90, vol. 47, no. 3, pp. 275–292.
13. Xia, Zh., Existence of Invariant Tori in Volume-Preserving Diffeomorphisms, *Ergodic Theory Dynam. Systems,* 1992, vol. 12, no. 3, pp. 621–631.
14. Cong, F., Li, Y., and Huang, M., Invariant Tori for Nearly Twist Mappings with Intersection Property, *Northeast. Math. J.,* 1996, vol. 12, no. 3, pp. 280–298.
15. Kaneko, K. and Bagley, R. J., Arnold Diffusion, Ergodicity and Intermittency in a Coupled Standard Mapping, *Phys. Lett. A,* 1985, vol. 110, no. 9, pp. 435–440.
16. Kantz, H. and Grassberger, P., Internal Arnold Diffusion and Chaos Thresholds in Coupled Symplectic Maps, *J. Phys. A,* 1988, vol. 21, no. 3, L127–L133.
17. Kook, H. and Meiss, J. D., Diffusion in Symplectic Maps, *Phys. Rev. A (3),* 1990, vol. 41, no. 8, pp. 4143–4150.
18. Honjo, S. and Kaneko, K., Is Arnold Diffusion Relevant to Global Diffusion?, arXiv:nlin/0307050 (2003).
19. Lega, E., Guzzo, M., and Froeschlé, C., Detection of Arnold Diffusion in Hamiltonian Systems, *Phys. D,* 2003, vol. 182, nos. 3–4, pp. 179–187.
20. Honjo, S. and Kaneko, K., Structure of Resonances and Transport in Multidimensional Hamiltonian Dynamical Systems, in *Geometric Structures of Phase Space in Multidimensional Chaos: Applications to Chemical Reaction Dynamics in Complex Systems: Part 2,* M. Toda, T. Komatsuzaki, T. Konishi, R. S. Berry, S. A. Rice (Eds.), Adv. Chem. Phys., vol. 130, Hoboken, N.J.: Wiley, 2005, pp. 437–463.
21. Guzzo, M., Lega, E., and Froeschlé, C., First Numerical Evidence of Global Arnold Diffusion in Quasi-Integrable Systems, *Discrete Contin. Dyn. Syst. Ser. B,* 2005, vol. 5, no. 3, pp. 687–698.
22. Froeschlé, C., Lega, E., and Guzzo, M., Analysis of the Chaotic Behaviour of Orbits Diffusing along the Arnold Web, *Celestial Mech. Dynam. Astronom.,* 2006, vol. 95, nos. 1–4, pp. 141–153.
23. Guzzo, M., Lega, E., and Froeschlé, C., First Numerical Investigation of a Conjecture by N. N. Nekhoroshev about Stability in Quasi-Integrable Systems, *Chaos,* 2011, vol. 21, no. 3, 033101, 12 pp.
24. Efthymiopoulos, C. and Harsoula, M., The Speed of Arnold Diffusion, *Phys. D,* 2013, vol. 251, pp. 19–38.
25. Cincotta, P., Efthymiopoulos, C., Giordano, C., and Mestre, M., Chirikov and Nekhoroshev Diffusion Estimates: Bridging the Two Sides of the River, *Phys. D,* 2014, vol. 266, pp. 49–64.
26. Pfenniger, D., Numerical Study of Complex Instability: P. 2. Barred Galaxy Bulges, *Astron. Astrophys.,* 1985, vol. 150, no. 1, pp. 112–128.
27. Jorba, À. and Ollé, M., Invariant Curves near Hamiltonian – Hopf Bifurcations of Four-Dimensional Symplectic Maps, *Nonlinearity,* 2004, vol. 17, no. 2, pp. 691–710.
28. Zachilas, L., Katsanikas, M., and Patsis, P. A., The Structure of Phase Space Close to Fixed Points in a 4D Symplectic Map, *Internat. J. Bifur. Chaos Appl. Sci. Engrg.,* 2013, vol. 23, no. 7, 1330023, 7 pp.
29. Cartwright, J. H. E., Feingold, M., and Piro, O., Chaotic Advection in Three-Dimensional Unsteady Incompressible Laminar Flow, *J. Fluid Mech.,* 1996, vol. 316, pp. 259–284.

30. Mezić, I., Break-Up of Invariant Surfaces in Action–Angle–Angle Maps and Flows, *Phys. D,* 2001, vol. 154, nos. 1–2, pp. 51–67.
31. Arnold, V. I., *Mathematical Methods of Classical Mechanics,* 2nd ed., Grad. Texts in Math., vol. 60, New York: Springer, 1997.
32. Kuksin, S. and Pöschel, J., On the Inclusion of Analytic Symplectic Maps in Analytic Hamiltonian Flows and Its Applications, in *Seminar on Dynamical Systems (St. Petersburg, 1991),* S. Kuksin, V. Lazutkin, J. Pöschel (Eds.), Progr. Nonlinear Differential Equations Appl., vol. 12, Basel: Birkhäuser, 1994, pp. 96–116.
33. Guzzo, M., A Direct Proof of the Nekhoroshev Theorem for Nearly Integrable Symplectic Maps, *Ann. Henri Poincaré,* 2004, vol. 5, no. 6, pp. 1013–1039.
34. Froeschlé, C., Lega, E., and Gonczi, R., Fast Lyapunov Indicators: Application to Asteroidal Motion, *Celestial Mech. Dynam. Astronom.,* 1997, vol. 67, no. 1, pp. 41–62.
35. Guzzo, M., Lega, E., and Froeschlé, C., On the Numerical Detection of the Stability of Chaotic Motions in Quasi–Integrable Systems, *Phys. D,* 2002, vol. 163, nos. 1–2, pp. 1–25.
36. Lega, E., Guzzo, M., and Froeschlé, C., Theory and Applications of the Fast Lyapunov Indicator (FLI) Method, in *Chaos Detection and Predictability,* Ch. Skokos, G. A. Gottwald, J. Laskar (Eds.), Lecture Notes in Phys., vol. 915, Berlin: Springer, 2016, pp. 35–54.
37. Gardner, E. S., Jr. Exponential Smoothing: The State of the Art: Part 2, *Int. J. Forecasting,* 2006, vol. 22, no. 4, pp. 637–666.
38. Dummit, D. S. and Foote, R. M., *Abstract Algebra,* 3rd ed., Hoboken, N.J.: Wiley, 2004.
39. Guillery, N. and Meiss, J., *Tech. Rep.,* University of Colorado, 2017 (in progress).
40. Lamb, J. and Roberts, J., Time-Reversal Symmetry in Dynamical Systems: A Survey, *Phys. D,* 1998, vol. 112, nos. 1–2, pp. 1–39.
41. Fox, A. M. and Meiss, J. D., Critical Invariant Circles in Asymmetric and Multiharmonic Generalized Standard Maps, *Commun. Nonlinear Sci. Numer. Simul.,* 2014, vol. 19, no. 4, pp. 1004–1026.
42. Kook, H. and Meiss, J. D., Periodic Orbits for Reversible, Symplectic Mappings, *Phys. D,* 1989, vol. 35, nos. 1–2, pp. 65–86.